Zirconium(IV)-Loaded Amino Functionalized Walnut Shell for Efficient Adsorption of Phosphate and 2,4-Dichlorophenoxyacetic Acid from Water

Xiaoxuan Ma[1] · Lihui Chen[1] · Evan Dovi[1] · Lingbo Qu[1] · Runping Han[1]

Abstract

A cost-effective adsorbent (AWS@Zr) was synthesized from walnut shell using Zirconium and amino group modification for the uptake of 2,4-dichlorophenoxyacetic acid (2,4-D) and phosphate (PO_4^{3-}). Characterization of the adsorbents revealed a significant difference in the physicochemical parameters of pristine and functionalized walnut shell. Langmuir model was observed to predict adsorption of 2,4-D, while Freundlich model best-fitted PO_4^{3-} adsorption with chemisorption being the principal underlying mechanism. The adsorption phenomena were pH dependent with Langmuir maximum capacity of 227.4 ± 5.4 mg g^{-1} and 73.9 ± 3.2 mg g^{-1} for 2,4-D and PO_4^{3-}, respectively. Kinetic models were also used to analyze the experimental data, and remarkable determined coefficients favor the pseudo-second-order kinetic model for the batch systems. The column experiments were carried out as a function of adsorbates flow rate, initial feed of 2,4-D and PO_4^{3-} concentration, bed depth. The results indicated both Thomas and Clark models could predict uptake of 2,4-D and phosphate with Thomas maximum capacity as 195.5 ± 1.0 for 2,4-D and 87.4 ± 0.7 mg g^{-1} for PO_4^{3-} at optimum flow rate of 10 mL min^{-1} and bed depth of 6 cm. Moreover, the column isotherm studies revealed that the Langmuir model predicted the adsorption data of PO_4^{3-}, and 2,4-D, which was consistent with batch adsorption of 2,4-D. The studied pollutants onto AWS@Zr are $PO_4^{3-} >$ 2,4-D based on the β^{-1} obtained from the column's mass transfer analysis. Adsorption–desorption studies revealed the reusability potentials of AWS@Zr. Zr and amino in surface of AWS@Zr play major role during removal of 2,4-D and PO_4^{3-}. There is potential for AWS@Zr to remove some anionic pollutants from solution.

Keywords Zr-loaded amino functionalized walnut shell · Adsorption · Phosphate · 2,4-Dichlorophenoxyacetic acid

Introduction

Water plays an integral role in human existence; accessibility to it is, therefore, critical. In spite of its status as a universal resource, water remains disproportionately available around the world. The pollution phenomenon caused by human activities has seriously impacted the supply and accessibility of safe and high-quality water [1]. Agricultural technology continues to develop to maintain food security on the globe, this leading to the introduction of new pest and weed control strategies and fertilizers to enhance food production. This has resulted in a more than 1.5-fold increase in pesticide usage globally during the last four decades, posing a significant environmental and health risk. These pollutants (such as pesticides, herbicides) have been shown to contaminate freshwater, decrease soil quality, and harmful to soil microorganisms. They may also enter the food chain and affect the ecosystem [2]. The most common chloro-organic herbicide, widely used due to its low cost and selectivity toward weeds during agriculture, is 2,4-dichlorophenoxy-acetic acid (2,4-D) [3]. The movement of 2,4-D, which is bio-accumulative throughout the food chain, with its residue traceable in various environmental media [4], poses a challenge to an aquatic organism [5], carcinogenic effect, and ability to disrupt endocrine. The World Health Organization (WHO) recommends a maximum allowable level of 100 μg L^{-1} for 2,4-D in drinking water.

✉ Lihui Chen
chenlh@zzu.edu.cn

✉ Runping Han
rphan67@zzu.edu.cn

1. College of Chemistry, Zhengzhou University, No 100 of Kexue Road, Zhengzhou 450001, People's Republic of China

Furthermore, phosphate is another pollutant that emerges during fertilization during the agricultural process. There is the permissible limit of 0.1 mg L^{-1} for phosphates in surface waters from USEPA (U.S. Environmental Protection Agency). The presence of excess phosphates may cause Eutrophication in water bodies and it is a worldwide environmental issue that has received increased attention in recent decades [6, 7]. Eutrophication may cause drastic reductions in dissolved oxygen (DO), the death of aquatic species, and the release of poisonous chemicals. As a result, eutrophication presents a major danger to human health and environmental quality [8]. Therefore, it is exigent to develop protocols to remove these pollutants from the environment effectively.

Presently, several decontamination techniques such as adsorption, electrolysis, coagulation/flocculation, membrane separation chemical oxidation, filtration and microbial degradation have been applied in wastewater management [9]. Again, all techniques applied for the removal of contaminants from wastewater demonstrate some degree of effectiveness, but they come with drawbacks such as high cost, complexity, and operator training requirements. Among them, the adsorption method is a favored technology because to its cheap starting cost, environmental friendliness, and increased efficiency [10, 11]. Again, in the adsorption studies, the most widely used and effective substance for removing pollutants is commercial activated carbon (CAC) or the alumina (Al_2O_3). However, they come with limitations such as high cost and difficulty of regeneration for spent adsorbent [12]. Hence, it is imperative to consider low-cost and high-efficient materials for the removal of toxic pollutants from wastewater. In recent years, agricultural-waste-materials as alternative low-cost adsorbents have been employed to remove various pollutants. But there is low adsorption capacity with direct use of these materials. Through modification, the adsorption capacity of the plant biomass can be enhanced [13, 14]. During chemical modified methods, amino introduction can change the functional groups and enhance the binding adsorption capacity towards heavy metal ions and anionic pollutant [10, 13]. Zirconium ions also can be introduced into surface of materials to improve the adsorption quality or selectivity of some pollutants [15, 16]. Zr is multivalent metal which is prevalent in the earth's crust, has the ability to form stable complexes with great selectivity for certain pollutants. As a consequence, it has lately received a lot of interest [17, 18].

In our previous study, one adsorbent based on the walnut shell (WS) was obtained by incorporating diethylenetriamine (DETA) and triethylamine (TEA), and Zr ions. The design process relies on amine groups' ability to form coordination bond with Zr(IV). Therefore, a coordination of zirconium onto an amine-grafted walnut shell (AWS@Zr) was developed as a functional adsorbent for the uptake of anionic dyes (Alizarin red, AR). There is good adsorption capacity and selection of AR while the mechanism of adsorption and antibacterial properties of adsorbent are performed [19].

In this study, AWS@Zr is used as adsorbent to remove chemical pollutants (phosphate and 2,4-D). The batch mode provides the necessary understanding of the adsorption process. It is, however, limited in terms of industrial use. Consequently, the continuous column mode was evaluated. Continuous contact between fresh contaminants and adsorbents is facilitated by the column adsorption process, resulting in higher removal efficiency. Again, a large amount of wastewater is purified in a short time. The study is performed: (i) to investigate the effect of several variables on the adsorption efficiency of studied pollutants; (ii) the isotherm, kinetics, and thermodynamic parameters of the removal process; (iii) the effect of column operating factors such as flow rate, column depth, and concentration on the breakthrough curves; (iv) analysis of column adsorption experimental results through employing Thomas, and Clark models; (v) studies of desorption to determine recycling potential of AWS@Zr.

Materials and Methods

Materials

The WS was acquired locally at Zhengzhou., potassium phosphate monobasic (KH_2PO_4), 2,4-dichlorophenoxyacetic acid (2,4-D), zirconium oxychloride octahydrate ($ZrOHCl_2 \cdot 8H_2O$) was purchased from Aladdin Reagent Co., Ltd., sodium hydroxide (NaOH), hydrochloric acid (HCl), *N*,*N*-dimethylformamide (DMF), triethylamine (TEA), Merck, epichlorohydrin (ECH), sodium sulphate (Na_2SO_4), sodium chloride (NaCl), and diethylenetriamine (DETA) were acquired from Zhengzhou Chemical Corporation, China. Chemicals and solvents used in all experiments were analytically graded without further processing.

Adsorbent Preparation

The AWS was synthesized as described in our previous studies [19]. The process of preparation as involves two parts. Part 1, 1.0 g of the ground walnut shell (40–60 mesh) was placed in a round bottom flask with 10 mL of ECH and 12 mL of DMF. The mixture was placed in an oil bath at 85 °C for 1 h with continuous stirring. 3.5 mL of DETA was then added and continually stirred for another 1 h. For the grafting process, 10 mL of TEA was added to the mixture at 85 °C with continuous stirring for 3 h. The amine grafted walnut shell was separated and rinsed until pH reached neutral. Part 2, the zirconium-loaded AWS was fabricated by immersing 1.0 g of AWS into 100 mL of 0.05 M $ZrOCl_2 \cdot 8H_2O$ solution in a conical flask, and the pH was

adjusted to about 9. In an orbital shaker, a flask containing the mixture was whirled at 303 K for 12 h. Then the adsorbent was filtered out of the solution, rinsed several times with ultrapure water, and the AWS@Zr obtained was dried at 60 °C. The final product is stored in an airtight glass bottle. Figure S1 shows the synthetic route for AWS@Zr.

Characterization of AWS@Zr

The functional groups present on AWS@Zr were assessed using Fourier-transform infrared at 4000–500 cm^{-1} (FTIR-Nicolet iS50, American). The crystalline structure of the AWS@Zr was investigated using powder X-ray diffraction (XRD, PANalytical, The Netherlands). In contrast, the appropriate surface area of AWS@Zr was determined using the Brunauer–Emmett–Teller technique (BET, ASAP2420-4MP, American). The morphology of AWS and AWS@Zr was verified by scanning electron microscopy (SEM, Hitachi Su8020, Japan). X-ray photoelectron spectroscopy (XPS, Escalab 250xi, England) was employed to confirm the functionalization and uptake procedure. The absorbance of the residual concentration was determined using visible spectrophotometry (Persee TU-1900, China). The point of zero charges (pHzpc) of AWS@Zr was established to determine the surface charge of materials. The procedure in detail is shown in Supported information.

Batch Adsorption Tests

The batch adsorption study using AWS@Zr as the adsorbent was carried out in a 50 mL Erlenmeyer flask. Several variables influencing adsorption quantity were investigated, including pH of a solution, interaction time, dosage, salt content, and temperature of uptake process. In this study, to evaluate the effect mass, different dosages of AWS@Zr (0.004, 0.006, 0.008, 0.01, 0.02, 0.03) for 2,4-D and (0.003, 0.005, 0.007, 0.01, 0.02, 0.03 g) for phosphate were employed while maintaining the temperature (303 K) and concentration of 2,4-D (100 mg L^{-1}) and phosphate (50 mg L^{-1}) constant. Again, at a constant concentration of adsorbates and AWS@Zr dosage (0.01 g), the effects of varying temperatures (293, 303, and 313 K) were investigated. Furthermore, the impact of different concentrations of adsorbates on maintaining a constant dosage of AWS@Zr (0.01 g) and temperature (303 K) was assessed. The effect of salt content on adsorption quantity was studied using Na$_2$SO$_4$, CaCl$_2$ and NaCl solutions (0.02, 0.04, 0.06, 0.08, 0.1 mol L^{-1}). A specified quantity of salt was introduced to conical flasks with 10 mL of adsorbates at a constant concentration of 2,4-D (100 mg L^{-1}) and phosphate (50 mg L^{-1}), followed by 0.01 g of AWS@Zr. All adsorption experiments were carried out at an agitating velocity of 130 rpm and varied interaction durations. The solutions

pH was altered to 3.0 (for both 2,4-D and phosphate) using 0.1 mol L^{-1} hydrochloric acid or sodium hydroxide solutions (except for the effect of solution pH) for the adsorption process. After the uptake process was completed, the AWS@Zr was filtered. The absorbance of the residual concentration of adsorbates in the filtrate was determined using a UV–Vis spectrophotometer (Persee TU-1900, with 1 cm cuvette) based on the Beer–Lambert equation at a maximum wavelength of 283 nm for 2,4-D and 700 nm for phosphate via Mo–Tb anti spectrophotometry. The experiments for adsorption performance were done twice and the average data were recorded (error less than 5%). The blank experiments were controlled using the mixtures solution without adsorbent or adsorbate.

$$P = \frac{(C_0 - C_e)}{C_0} \times 100\%, \tag{1}$$

$$q_e = \frac{(C_0 - C_e)V}{W}. \tag{2}$$

Desorption of 2,4-D and Phosphate from AWS@Zr in Batch Studies

Desorption in the batch mode was conducted to determine the constancy and reusability of the AWS@Zr after the 2,4-D and phosphate uptake. The study evaluated three different desorption solutions: NaOH, HCl, and NaOH–NaCl, with a concentration of 0.1 mol L^{-1} each. At the same experimental conditions AWS@Zr was loaded with a 10 mL adsorbate solution. The loaded AWS@Zr samples were separated, rinsed, and dried in an oven for 12 h at 60 °C. The dried spent AWS@Zr was placed into a flask containing 10 mL of the desorption solvents for a duration of 2 h for 2,4-D loaded adsorbent and 3 h for phosphate loaded adsorbent. The adsorption and desorption cycles were repeated three consecutive times. The efficiency of desorption and regeneration was obtained using q_e before and after desorption.

Column Studies

At 303 K and pH 3.0 for both pollutants the column uptake test was conducted using an AWS@Zr packed column with an internal diameter of 1.3 cm, a glass tube length of 30 cm, and a bed depth of 3 cm (0.930 g), 6 cm (1.86 g), and 9 cm (2.79 g). The bottom of the column is equipped with a stainless steel screen with a cotton film, which plays a supporting role and avoids the leakage of the adsorbent. The test is performed using a peristaltic pump to feed the solutions into the column in a downward flow mode. The outlet solutions were taken periodically during the uptake process.

Column Data Analysis

The period required for a breakthrough to occur and the shape of the breakthrough curve are vital factors in defining uptake's functional and kinetic characteristics in a fixed-bed column. The loading behavior of pollutants removed from solution in a fixed-bed column is depicted as breakthrough curves, typically represented in terms of normalized concentration as the time-dependent ratio of outlet adsorbates concentration to inlet adsorbates concentration (C_t/C_0). The mass of adsorbates adsorbed, q_{total} (mg), could be evaluated by analyzing the region under the breakthrough curve (Eq. 3) and the column's adsorption capacity, q_{exp} (mg g^{-1}), is computed with Eq. (4).

$$q_{total} = \frac{v}{1000} \int_{t=0}^{t=t_{total}} (C_0 - C_t) dt, \tag{3}$$

$$q_{exp} = q_{total}/x, \tag{4}$$

where C_0 is the adsorbate concentration (mg L^{-1}), v is the flow rate (mL min^{-1}), x is the dried mass of AWS@Zr in the tube (g). The mass transfer (MF) factor was computed to assess the column potential and the affinity between adsorbates and AWS@Zr using the modified mass transfer factor (MMTF) model, Eq. (5) [20].

$$\ln \frac{C_0}{C_t} = [K_L a]_g \times e^{-\beta \times \ln q} \times t, \tag{5}$$

where $[K_L a]_g$ (h^{-1}) is the global MF coefficient, β^{-1} (g h mg^{-1}) is the affinity between adsorbates and AWS@Zr, and t is the period of the experimental phase (h). A graph obtained from Eq. (6) yielded a straight line.

$$\ln q \frac{1}{\beta} \times \ln t + B, \tag{6}$$

$$B = \frac{\ln([K_L a]_g) - \ln\left[\ln \frac{C_0}{C_t}\right]}{\beta}, \tag{7}$$

where B is the MF index, related to the driving force during adsorbates adsorption (mg g^{-1}).

Column Adsorption Kinetic Models

The development and optimization of a column removal system's breakthrough curve need a simple modelling method to simulate the flow behavior. In this work, the Thomas and Clark model was used to analyze the dynamic behavior of the column.

Thomas Model Application The Thomas model is employed to estimate the breakthrough curve in dynamic flow phenomena [21]. It is based on the premise that the driving force's reaction rate obeys second-order reversible reaction kinetics. This model equation is denoted by the following:

$$\frac{C_t}{C_0} = \frac{1}{1 + \exp(k_{Th} q_0 x/v - k_{Th} C_0 t)}. \tag{8}$$

Clark Model Application The Clark model is used in conjunction with the Freundlich isotherm to define a relationship for the breakthrough curve, and the model is expressed as following [22].

$$\frac{C_t}{C_0} = \left(\frac{1}{1 + Ae^{-rt}}\right)^{1/(n-1)}, \tag{9}$$

where C_0 and C_t denote the inlet and outlet concentration (mg L^{-1}), respectively; k_{Th} is constant for the Thomas model (mL min^{-1} mg^{-1}), q_0 represents the maximum amount adsorbed (mg g^{-1}), x is the mass of AWS@Zr (g), and v is the feed rate (mL min^{-1}); Clark constants A and r, Freundlich parameter, n is 3.77 (PO$_4^{3-}$) and 3.69 (2,4-D) derived from the batch mode. A plot of C_t/C_0 versus t at different conditions was used to estimate the Clark constants.

Results and Discussion

Adsorbent Characterization

The SEM pictures of AWS and AWS@Zr are shown in Fig. 1a and b, respectively. It clearly shows that the surface morphology of AWS changed drastically; the surface looked more porous after modification. The changes observed could illustrate the successful loading of zirconium metal onto AWS. The uniform rough surface of AWS@Zr could have aided the removal potential.

Figure 1c depicts the FT-IR spectra of AWS@Zr. The broad around 3300–3400 cm^{-1} corresponds to the stretching and bending vibration bonds of –OH due to a large number of hydroxyl groups and H$_2$O molecules present on the adsorbents. The absorption peaks observed around 2900 cm^{-1} on the adsorbents could be credited to the presence of CH$_2$ groups. Again, the adsorption peak on AWS@Zr around 1334 cm^{-1} matched up to C–N bending vibrations, indicating the presence of amine groups [23]. The emergence of a new peak at 2838 cm^{-1} and at 1739 cm^{-1} was found on AWS as reported in our previous studies [19] shifted slightly to 1730 cm^{-1} shown on AWS@Zr resulted after loading Zr ion.

The XRD analysis is performed in our previous studies [19]. XRD peak position of the precursor (WS), which
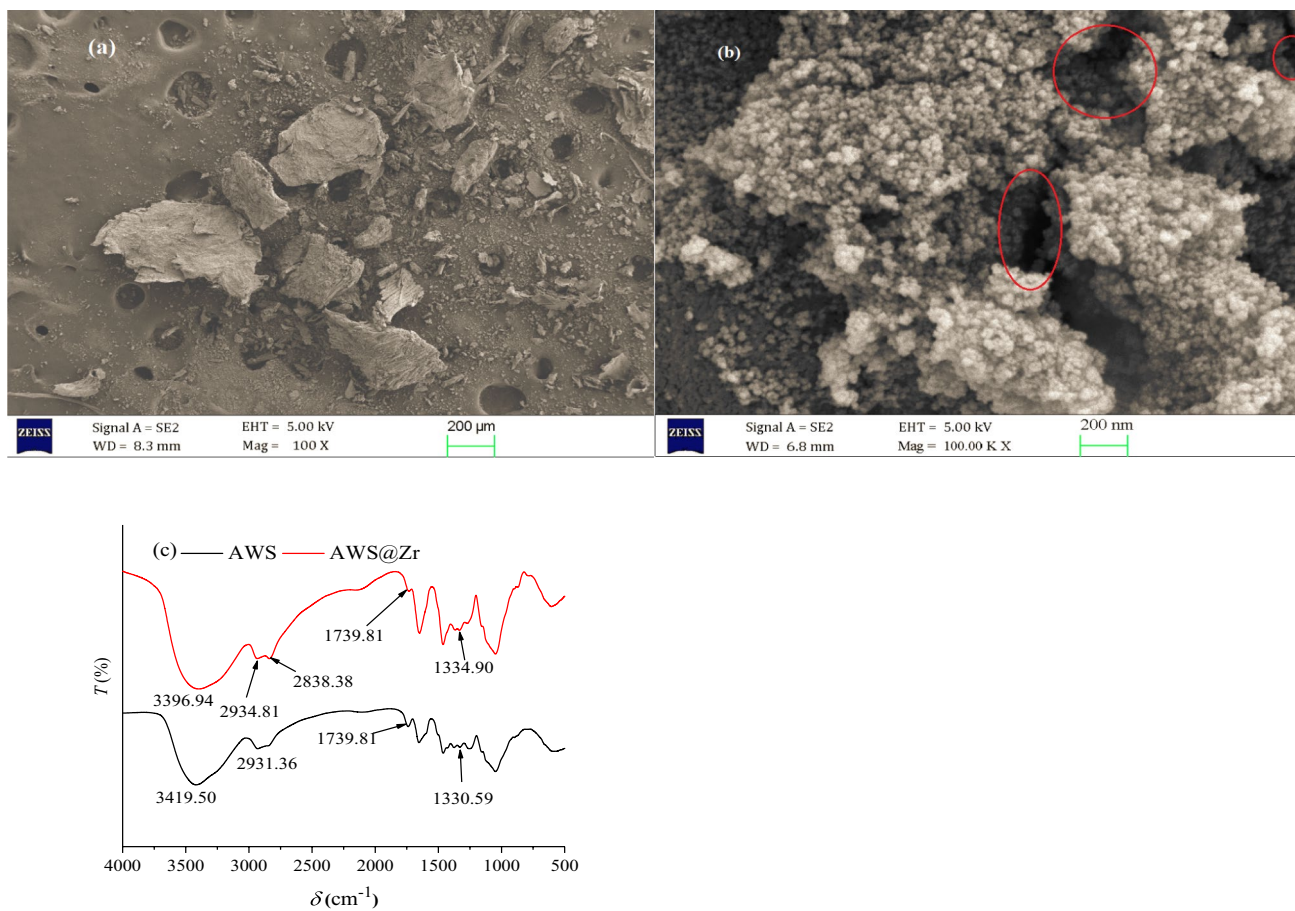
Fig. 1 SEM images showing the morphology of AWS (**a**) and AWS@Zr (**b**); FT-IR spectra of AWS and AWS@Zr-AR (**c**)
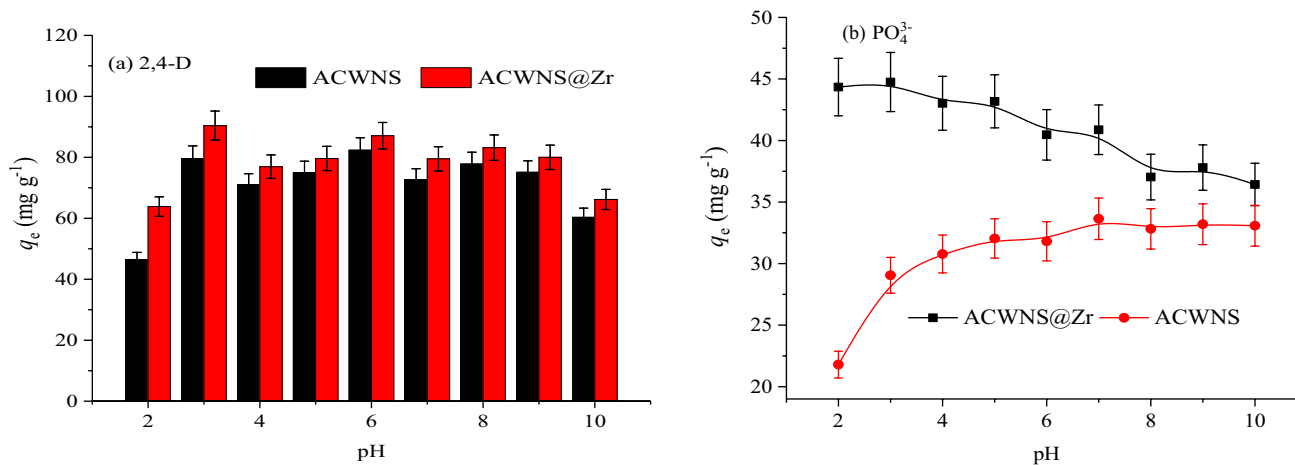
Fig. 2 Influence of pH on adsorption of **a** 2,4-D ($C_0 = 100$ mg L^{-1}, $T = 303$ K, $t = 3$ h) and **b** PO$_4^{3-}$ ($C_0 = 50$ mg L^{-1}, $T = 303$ K, $t = 2$ h)

is around $2\theta = 17.5°$, $22.5°$, and $35°$, changed slightly in the intermediate (AWS) and the final product (AWS@Zr), as a result of the modification process, but the organized crystal cellulose structure remained [24]. Similar peaks on AWS and AWS@Zr were observed at $2\theta = 21.88°$ and $35°$. This implied that the modification did not alter the crystalline structure of cellulose existed in the precursor (WS).

The BET study was performed to describe the surface characteristics of AWS@Zr, and the findings were likened to its precursor (WS) and intermediate product (AWS). Figure S2 depicts the graph obtained from the adsorption and desorption of N_2 gas on the surface of AWS. AWS@Zr has a surface area of 0.327 m^2 g^{-1}, whereas WS and AWS have surface areas of 0.230 and 0.369 m^2 g^{-1}, respectively, as reported in our earlier studies [19]. The total pore volume of AWS decreased from 0.00301 to 0.000848 cm^3 g^{-1} (AWS@Zr) after modification. The average pore width from 32.7 nm (AWS) reduced to 10.4 nm (AWS@Zr), showing the mesoporous structure. The reduction is due to the Zr plugging the pores on the surface of adsorbent.

Adsorption Study

Influence of pH on Adsorption of 2,4-D and Phosphate

The pH value of the solution is critical to the adsorption mechanism because it affects the functional groups present on the surface of the adsorbent and the substances present in the adsorbent. Phosphate exists in three main forms: H_3PO_4, $H_2PO_4^-$, and HPO_4^{2-} with pK_a values of 2.17, 7.20, and 12.37, respectively [25]. As reported, within this pH range of 3–10, phosphates are likely to exist in $H_2PO_4^-$ and HPO_4^{2-} which are strongly attracted to the positively charged adsorbent; with this attraction decreasing with an increase in solution pH [25]. Figure 2a and b illustrate the effect of pH on the adsorption of 2,4-D, and phosphate on AWS@Zr, respectively. As depicted in Fig. 2a and b, it is clear that higher pH (alkaline medium) negatively affected the adsorption processes for 2,4-D, and phosphate. However, when the solution pH rose from 2 to 10, the adsorption capacity (q_e) of AWS@Zr for phosphate declined from 44.2 to 36.4 mg g^{-1}, while the adsorption capacity of 2,4-D decreased from 90.4 to 66.2 mg g^{-1}. The reduction in the adsorption capacity could stem from the competitive effect of increased hydroxide ions at higher pH. Again, the point of zero charges of AWS@Zr was recorded as 6.7 (figure not shown). This implies that when the pH value is below pHzc, the adsorbent's surface becomes positive due to the protonation of the active groups available on AWS@Zr [16]. Consequently, the adsorbent and negatively charged phosphate and 2,4-D ions have improved electrostatic interactions, augmenting the uptake capacity of AWS@Zr. There is still good adsorption capacity at pH 10, this shows that maybe there is H-bond or complexation between adsorbates and adsorbents. For AWS, as there is not complexation between AWS and PO_4^{3-}, the trend of curve in Fig. 2b is opposite. Hence, pH 3 was employed for adsorption of phosphate and 2,4-D.

Effect of Adsorbent Dose

The influence of various mass of AWS@Zr (0.003–0.030 g) on the adsorption of 2,4-D and PO_4^{3-} have been examined. The experiment was carried out at pH 3, 2 h and concentrations of 100 mg L^{-1} for 2,4-D and at pH 3, 3 h and concentration of 50 mg L^{-1} for PO_4^{3-}. Figure S3a and b depict the impact of mass on the adsorbate removal phenomenon. Increasing the mass of AWS@Zr from 0.003 to 0.03 g increased the removal efficiency from 71.9 to 95.1% for 2,4-D and 75.4–99.3% for PO_4^{3-}. These results might have stemmed from a high number of accessible binding sites. Alternatively, q_e for the adsorption of the adsorbates reduced from 178.9–31.4 mg g^{-1} for 2,4-D and 125.2–16.3 mg g^{-1} for PO_4^{3-} as the mass of AWS@Zr increased, resulting from underutilized active sites in the removal phenomenon, as depicted in Fig. 3. In comparison to AWS@Zr, AWS exhibited decreased adsorption efficiency, as presented in Fig. 2a for 2,4-D and Fig. 2b for PO_4^{3-}. PN–Fe$_3$O$_4$–IDA–Zr from another study exhibited similar enhanced adsorption capacity towards phosphate [15]. In their work, the q_e of PN–Fe$_3$O$_4$–IDA–Zr was about 5.5 mg g^{-1}, whereas the q_e of PN–Fe$_3$O$_4$–IDA was 2.0 mg g^{-1}. The increased adsorption indicates that the zirconium metal ion loaded onto the adsorbents considerably contributed to the removal efficiency. From Figs. S3a and 2b, the percentage removal at a mass of 0.01 g was greater than 90% for all the adsorbates while their q_e recorded were relatively higher; hence, 0.010 g of AWS@Zr was utilized as the optimal dose for the work.

Effect of Salinity

Salt ions are one of the many components accompanying effluents emanating from most industries. Hence, it is vital to assess the impact of salt ions on the uptake phenomena. In this experiment, NaCl, CaCl$_2$ and Na$_2$SO$_4$ effects on the absorption of the adsorbate were evaluated. As shown in Fig. S3c and d, the uptake capacity of AWS@Zr declined as the NaCl and Na$_2$SO$_4$ content rose from 0.02 to 0.1 mol L^{-1}. This phenomenon may be attributed to the competitive effect of Cl$^-$ and SO$_4^{2-}$ ions on the 2,4-D and phosphate of the active groups present on AWS@Zr, limiting their absorption. This indicates that electrostatic interaction may have acted as the underlying adsorption mechanism.

Furthermore, in solution, salt cations (Na$^+$ and Ca^{2+}) may demonstrate competitive adsorption behavior with cationic AWS@Zr to bind with negative 2,4-D. During this occurrence, it seems that some of the 2,4-D molecules interacted with salt cations, producing a negative effect [26]. This outcome reduces the probability of 2,4-D being binding to AWS@Zr. CaCl$_2$ had the greatest effect on the q_e of AWS@Zr among the salts, as seen in Fig. S3c. This
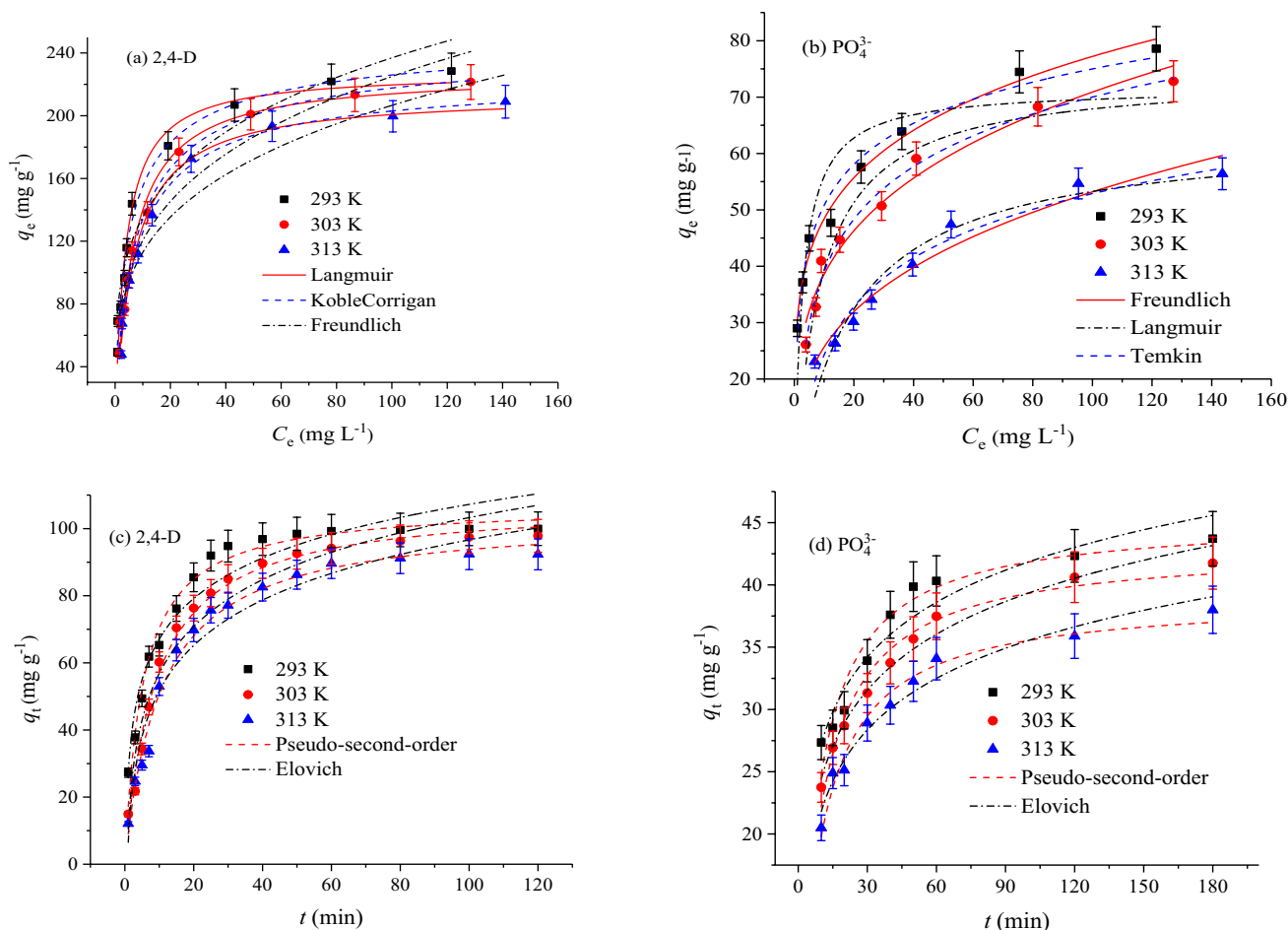
Fig. 3 fitted curves for adsorption isotherm **a** 2,4-D ($C_0 = 50$–350 mg L^{-1}, $t = 2$ h, pH 3, $m = 0.010$ g) and **b** PO$_4^{3-}$ ($C_0 = 30$–200 mg L^{-1}, $t = 3$ h, pH 3, $m = 0.010$ g); Fitted curves for adsorption kinetics **c** 2,4-D ($C_0 = 100$ mg L^{-1}, $t = 2$ h, pH 3, $m = 0.010$ g) and (d) PO$_4^{3-}$ ($C_0 = 50$ mg L^{-1}, $t = 3$ h, pH 3, $m = 0.010$ g)

result might be due to calcium ion (Ca^{2+}) having a larger charge density than sodium ion (Na$^+$). Therefore, there was greater competitive interaction between Ca^{2+} and AWS@Zr than Na$^+$ and AWS@Zr.

Influence of Concentration and Application of Isotherm Models

The impact of different concentrations of PO$_4^{3-}$ and 2,4-D were studied at varying temperatures (293, 303, and 313 K) to assess the removal efficiency of the prepared adsorbent (AWS@Zr). Figure 3a and b depicts the outcome of the removal efficiency of the adsorbent. It was observed from these figures that at higher concentrations, q_e increased proportionally. An increase in adsorbate concentration offered the needed driving force to enhance the mass transfer effect. The experimental q_e values for PO$_4^{3-}$ and 2,4-D adsorption increased at lower

temperatures, implying an exothermic reaction for both PO$_4^{3-}$ and 2,4-D adsorption. Adsorption isotherms, which are mathematical expressions, aid in determining the interactions between adsorbent and adsorbate molecules at equilibrium, the details regarding the adsorbent's surface properties and adsorption mechanism [27]. In this work, the Langmuir (Eq. 10), Freundlich (Eq. 11), Temkin (Eq. 12) and the Koble–Corrigan (Eq. 13) isotherm models were employed to describe the experimental data at different temperatures. The relevant parameters obtained by the nonlinear regression analysis of the three models (Langmuir, Freundlich, Temkin models) for PO$_4^{3-}$ and (Langmuir, Freundlich, Koble–Corrigan models) for 2,4-D experimental data are shown in Table 1. The expressions of models are as follows:
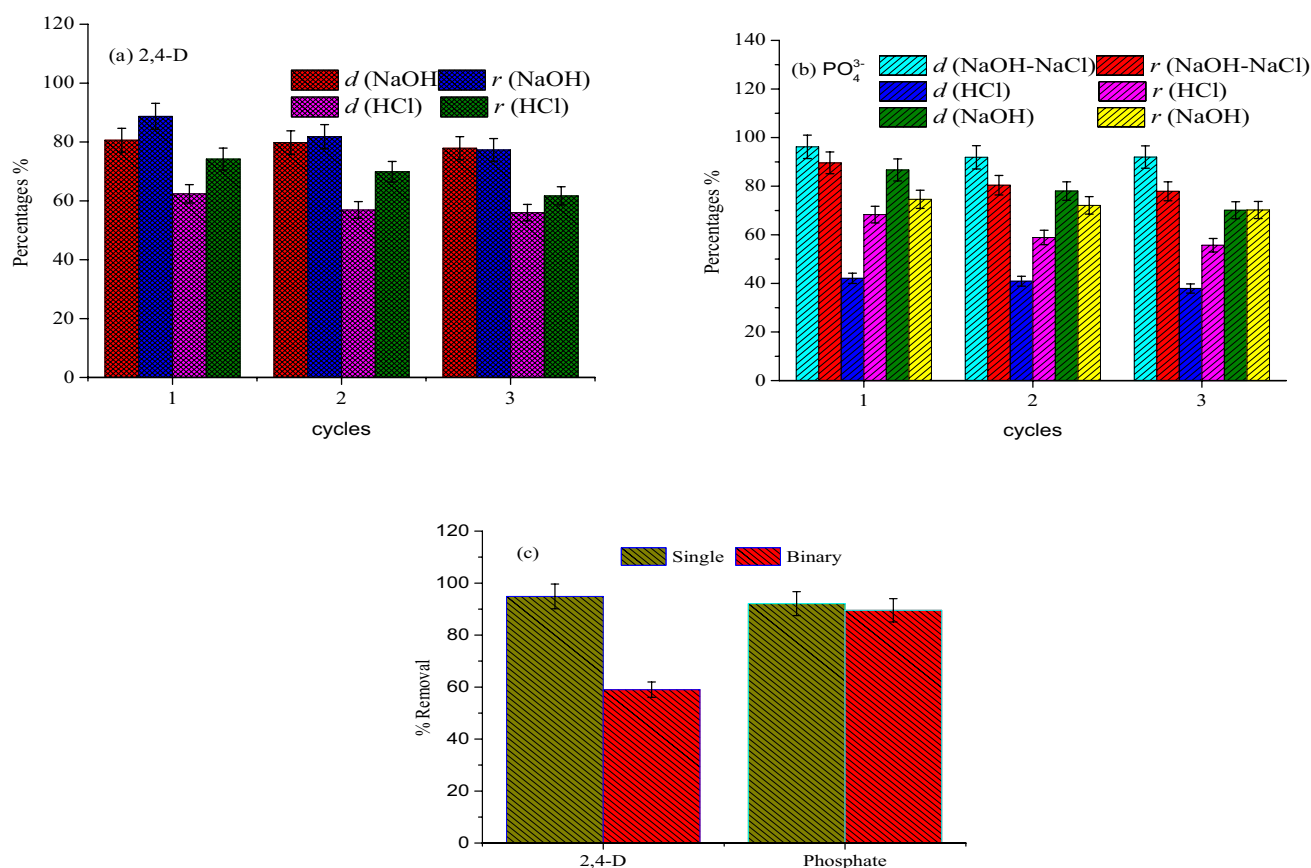
$$q_e = \frac{q_m K_L C_e}{1 + K_L C_e}, \tag{10}$$

Fig. 4 Desorption and regeneration efficiencies of AWS@Zr **a** 2,4-D, **b** PO_4^{3-} and **c** adsorption capacity of AWS@Zr for 2,4-D and PO_4^{3-} in single and binary systems (1:1 initial concentration, 50 mg L^{-1}; $T = 303$ K; $t = 3$ h; dose = 0.01 g)

$$q_e = K_F C_e^{1/n}, \tag{11}$$

$$q_e = A + B \ln C_e \tag{12}$$

$$q_e = \frac{AC_e^n}{1 + BC_e^n}, \tag{13}$$

The fitting curves of the experimental data are shown in Fig. 3a and b. According to the R^2 and *SSE* values, it points out that both the Freundlich and Temkin can predict the uptake phenomena for phosphate as shown in Table 1 and Fig. 3b. This result suggests that the adsorption process led to multilayer formation on heterogeneous surfaces and ion exchange [17]. The adsorption of phosphate onto AWS@Zr seems complex, involving more than one mechanism.

For the uptake of 2,4-D, the Koble-Corrigan model, a three-parameter model, which incorporates the features of Langmuir and Freundlich models for predicting the uptake of adsorbates onto heterogeneous systems, exhibited the highest correlation coefficient and the lowest SSE values

($R^2 = 0.986$–0.991, SSE = 2.47–4.53) compared to other isotherm models as illustrated in Table 1. Conversely, the recorded 'n' values were less than 1, indicating that the model could not predict the observed values regardless of its high R^2 and low SSE values. The assumption supports the concept that for the Koble–Corrigan equation to be valid, 'n' values must be greater or equal to unity [28].

Besides, the Langmuir model provided a good fit for experimental points based on the R^2 and SSE values; the closeness of the model fitted curves and the experimental data as depicted in Table 1 and Fig. 3a, respectively. Langmuir isotherm fitting indicates a homogenous distribution of adsorbate on the binding sites present on the surface of AWS@Zr. As reported by Han group [29], the Langmuir model has been determined to be the most often employed isotherm for the adsorption of a solute from a liquid solution owing to its suitability to a variety of pollutants adsorption processes. The Langmuir adsorption is premised on four hypotheses: (i) the adsorption sites on the surface are equal; they all have an equal probability of being occupied throughout the adsorption process; (ii) there exists no interaction between adsorbed molecules, (iii) the mechanism of uptake

Table 1 Isotherm parameters for PO_4^{3-} and 2,4-D adsorption onto AWS@Zr at different temperatures

Models/adsorbate	Parameters	293 K	303 K	313 K
PO_4^{3-}				
Langmuir	q_m (mg g^{-1})	71.5 ± 4.7	73.9 ± 3.2	63.5 ± 3.6
	K_L (L mg^{-1})	35.7 ± 0.1	11.3 ± 1.8	5.22 ± 0.91
	R^2	0.805	0.948	0.938
	$SSE \times 10^2$	3.62	0.858	0.599
Freundlich	K_F (mg g^{-1}) (L mg^{-1})$^{1/n}$	30.3 ± 1.10	20.9 ± 1.60	12.4 ± 1.3
	$1/n$	0.203 ± 0.010	0.265 ± 0.020	0.317 ± 0.026
	R^2	0.986	0.966	0.960
	$SSE \times 10^2$	0.247	0.550	0.394
Temkin	A	26.5 ± 1.9	8.03 ± 2.1	-4.44 ± 3.5
	B	10.5 ± 0.63	13.5 ± 0.63	12.4 ± 0.97
	R^2	0.975	0.985	0.959
	$SSE \times 10^2$	0.462	0.245	0.399
2,4-D				
Langmuir	q_m (mg g^{-1})	227.9 ± 7.1	227.4 ± 5.4	213.9 ± 5.0
	K_L (L mg^{-1})	0.266 ± 0.032	0.159 ± 0.014	0.153 ± 0.013
	R^2	0.972	0.985	0.984
	$SSE \times 10^2$	9.88	4.83	4.41
Freundlich	K_F (mg g^{-1}) (L mg^{-1})$^{1/n}$	77.4 ± 7.3	64.5 ± 6.9	61.7 ± 7.1
	$1/n$	0.242 ± 0.025	0.271 ± 0.028	0.262 ± 0.029
	R^2	0.927	0.928	0.915
	$SSE \times 10^2$	26.13	23.65	24.17
Koble–Corrigan	A	76.5 ± 7.1	46.8 ± 4.9	40.3 ± 5.6
	B	0.302 ± 0.027	0.190 ± 0.016	0.178 ± 0.021
	n	0.717 ± 0.090	0.798 ± 0.075	0.844 ± 0.095
	R^2	0.986	0.991	0.987
	$SSE \times 10^2$	4.53	2.47	3.21

Table 2 Comparison of studied pollutants removal capacity using AWS@Zr with other adsorbents

Adsorbents	q_m (mg g^{-1})	T (K)	References
2,4-D			
Yam peels activated carbon	99.0	298	[34]
Aminosilane-grafted mesoporous car	192.0	333	[35]
Commercial activated carbon	178.6	283	[36]
Ethylenediamine modified poly(glycidyl methacrylate) resin	99.5	298	[37]
Magnetic graphene	32.3	303	[38]
AWS@Zr	227.1	303	This study
PO_4^{3-}			
Wood fiber treated with ferrous chloride	5.3		[39]
Zr-loaded carbon nanotubes	10.9		[33]
Iminodiacetic acid/iron(III) functionalized magnetic peanut husk	33.7	308	[40]
Mn/Al double oxygen biochar	26.3		[41]
Zr-PEI-magnetic peanut husk	36.6	303	[42]
AWS@Zr	73.9	303	This study

is the same at all binding sites, (iv) there is the formation of a monolayer of the adsorbates on the surface of the adsorbent at equilibrium. The results have been compared to the uptake capacity of different adsorbents for the investigated contaminants, as shown in Table 2. It was observed that AWS@Zr has a higher adsorption capacity than previously reported absorbents.

Effect of Contact Time and Application of Kinetic Models

The influence of contact time was studied to explore the rate mechanism behind the removal process, and the fitting of kinetic models to curves is presented in Fig. 3c–d. In all cases, the reaction proceeded through two main kinetic phases: a rapid initial phase mediated by external mass transfer and a slower phase leading to equilibrium, controlled by intra-particle diffusion. It was evident from the figures that different adsorption processes reached equilibrium at different periods, which could be ascribed to the size of the adsorbate and the type of interactions that occur during the adsorption process. Kinetic models are fitted to experimental results to provide parameters useful for modelling and designing adsorption processes. Two nonlinear kinetic models: the pseudo-second-order kinetic model (Eq. 14) [30] and the Elovich equation (Eq. 15) [31], were fitted to the experimental data to comprehend the rate mechanism that underlines the reaction process.

$$q_t = \frac{k_2 q_e^2 t}{1 + k_2 q_e t}, \tag{14}$$

$$q_t = A + B \ln t \tag{15}$$

Figure 3c and d depict the fitted curves for data obtained from the adsorption 2,4-D, and PO_4^{3-}, respectively, whiles Table 3 shows the values for the kinetics models parameters attained. From Table 3, it can be inferred that the pseudo-second-order equation better describes the uptake of the studied pollutants onto the AWS@Zr surface, based on a higher regression coefficient (R^2) and lower error values (*SSE*) recorded. The fitted curves from the pseudo-second-order equation are closer to experimental points. These findings suggest that the chemisorption process could be the most probable underlying reaction mechanism in the uptake process, which is most plausible to be an electrostatic attraction [32]. Moreover, for the uptake of PO_4^{3-} the Elovich model also presented R^2 values, which were significant coupled with low SSE values, as illustrated in Table 3, indicating that the Elovich model could also predict the uptake of PO_4^{3-} onto AWS@Zr. These findings could further conjecture that the chemisorption reaction is most likely to govern the adsorption process, as a principal underlying reaction mechanism is dominated by coordination. Similar outcomes were reported by Gu et al. [33] and Hu and Han [18] in their respective studies.

Competitive Adsorption Studies

Phosphate and 2,4-D are chemicals employed during agricultural activities to enhance productivity. Hence, the chance for them co-existing in wastewater system is very

Table 3 Parameters of kinetic studies for 2,4-D, and PO_4^{3-} uptake onto AWS@Zr

T/K	293 K	303 K	313 K
2,4-D			
Pseudo-second-order			
$k_2 \times 10^{-5}$ (g mg^{-1} min^{-1})	17.9 ± 1.8	10.5 ± 0.84	9.23 ± 0.88
$q_{e(theo)}$ (mg g^{-1})	107.0 ± 2.0	107.9 ± 1.8	103.6 ± 2.1
R^2	0.976	0.990	0.987
$SSE \times 10^2$	1.91	1.03	1.26
Elovich equation			
$-A$	26.9 ± 4.0	10.4 ± 4.0	6.54 ± 3.70
B	17.4 ± 1.2	20.2 ± 1.2	19.6 ± 1.1
R^2	0.935	0.951	0.955
$SSE \times 10^2$	5.20	5.12	4.44
PO_4^{3-}			
Pseudo-second-order			
$k_2 \times 10^{-5}$ (g mg^{-1} min^{-1})	0.265 ± 0.038	0.247 ± 0.026	0.264 ± 0.027
$q_{e(theo)}$ (mg g^{-1})	45.3 ± 1.1	43.0 ± 0.8	39.0 ± 0.73
R^2	0.943	0.970	0.973
$SSE \times 10^2$	15.4	7.96	6.09
Elovich equation			
$-A$	12.6 ± 2.4	9.47 ± 1.20	8.06 ± 1.50
B	6.36 ± 0.63	6.49 ± 0.33	5.97 ± 0.40
R^2	0.926	0.980	0.965
$SSE \times 10^2$	19.8	5.42	8.10

high. It is therefore necessary to assess efficiency of developed adsorbents in competitive adsorption of Phosphate and 2,4-D. The experimental findings of adsorption in a binary system are shown in Fig. 4c. It was observed from Fig. 4c that when both phosphate and 2,4-D were present in solution, reduction in removal efficiency towards 2,4-D was observed, while affinity towards phosphate remained barely unchanged. The interference of phosphate on the adsorption of 2,4-D was considerable leading to a decrease in the removal potential of 2,4-D (from 94.9 to 59.0%). However, the addition of 2,4-D had only a minimal effect on phosphate adsorption, culminating in a slight reduction in its adsorption efficiency. As a basis of these observations, it can be deduced that AWS@Zr exhibited a stronger affinity for binding to phosphate with a higher degree of selectivity than 2,4-D.

Desorption and Regeneration Studies

A regeneration study was performed to investigate the effectiveness and reusability of adsorbents and this can enhance

the value of adsorbent [43–45]. In this study, 0.1 mol L^{-1} of desorbing agents (NaOH, NaOH-NaCl, and HCl) were employed. For 2,4-D-loaded AWS@Zr, the desorption and regeneration rate were (56–62.2%) and (74.3–61.7%) for HCl and (80.5–77.6%) and (88.5–77.3%) for NaOH, respectively. It is evident that a higher desorption rate seems to have occurred in alkaline than in the acidic condition for 2,4-D-loaded AWS@Zr as depicted in Fig. 4a.

The OH$^-$ ions in NaOH strongly obstructed the bond between AWS@Zr and the adsorbate (2,4-D), causing bond breaking, leading to the release of 2,4-D molecules from AWS@Zr into the medium. Furthermore, for the desorption of the PO$_4$$^{3-}$ loaded-AWS@Zr, the effectiveness of the desorbing agents follows the order NaOH-NaCl > NaOH > HCl as illustrated in Fig. 4b. The uptake capacity of AWS@Zr was relatively low in an alkaline medium (seen Fig. 2b), hence NaOH-NaCl was adopted to desorb PO$_4$$^{3-}$ loaded-AWS@Zr. Thus, suggesting that the presence of abundant OH$^-$ and Cl$^-$ in solution could interrupt the interactions that occur between the phosphate ions and the binding sites on AWS@Zr, leading to a greater phosphate ion desorption rate. This result might be explained using the ion exchange concept between the negative ions in the solution and the PO$_4$$^{3-}$ ions on the surface of AWS@Zr [33]. This phenomenon results in the release of phosphate ions into the solution and the liberating active sites for subsequent adsorption cycles. The findings of all investigations employing 2,4-D, and PO$_4$$^{3-}$ show that the AWS@Zr is highly reusable for further adsorption process and might serve as a feasible material for decontaminating and treating wastewater.

Thermodynamic Studies

To study the impact of temperature on the uptake of adsorbate by AWS@Zr, thermodynamic parameters such as Gibbs free energy ($\Delta G°$) (Eq. 17), enthalpy change ($\Delta H°$) (Eq. 18), and entropy change ($\Delta S°$) (Eq. 18) are estimated employing the following equations.

$$K_c = C_{ade}/C_e \tag{16}$$

$$\Delta G° = -RT \ln K_c, \tag{17}$$

$$\Delta G° = \Delta H° - T\Delta S°, \tag{18}$$

where K_c is the thermodynamic equilibrium constant that is dimensionless, C_{ade} is the 2,4-D and PO$_4$$^{3-}$ concentration on AWS@Zr at equilibrium (mg L^{-1}), C_e is the 2,4-D and PO$_4$$^{3-}$ concentration at equilibrium (mg L^{-1}) T (K) is the absolute temperature in Kelvin; R (8.314 J mol^{-1} K^{-1}) is the ideal gas constant. The value of $\Delta H°$ is enthalpy, and $\Delta S°$ is the degree of randomness. The entropy change demonstrates that 2,4-D and PO$_4$$^{3-}$, adsorption enhanced the

Table 4 Thermodynamic parameters for the uptake of studied pollutants on AWS@Zr

	$\Delta H°$ (kJ mol^{-1})	$\Delta S°$ (kJ mol^{-1} K^{-1})	$\Delta G°$ (kJ mol^{-1})		
			293 K	303 K	313 K
2,4-D	− 38.6	− 0.0981	− 9.88	− 8.68	− 7.93
PO$_4$$^{3-}$	− 82.3	− 0.254	− 8.18	− 4.80	− 3.14

degree of freedom at the solid–liquid interface. As depicted in Table 4, $\Delta G°$ values are negative at all temperatures for the studied pollutants, indicating a spontaneous adsorption process. For the uptake of 2,4-D and PO$_4$$^{3-}$, the absolute values of $\Delta G°$ decreased as temperature increased, signifying that lower temperature is preferable for the adsorption of 2,4-D and PO$_4$$^{3-}$. Moreover, the negative $\Delta H°$ as depicted in Table 4 for 2,4-D and PO$_4$$^{3-}$, represents exothermic adsorption phenomena. The magnitude of the $\Delta H°$ values for 2,4-D and PO$_4$$^{3-}$ suggest chemisorption process to be the dominant reaction mechanism [15]. Furthermore, the entropy of the aqueous interface during the uptake process decreased, depicting negative $\Delta S°$ values for 2,4-D and PO$_4$$^{3-}$ uptake (Table 4) [36].

Column Performance at Varied Operating Conditions

Influence of Flow Rate on Breakthrough Curves

Figure 5a and b shows the breakthrough curves at various flow rates, constant inlet 2,4-D (100 mg L^{-1}) and PO$_4$$^{3-}$ (50 mg L^{-1}) concentrations, and bed depth (6 cm). The curves demonstrate that the breakthrough and exhaustion times rose when the flow rate was reduced. As the flow rate was raised from 6 to 14 mL min^{-1}, the slope of the plots from breakthrough time to exhaustion time increased, indicating that the breakthrough curve becomes steeper as the flow rate increases. A lower flow rate leads to a longer residence period in the column and vice versa (Fig. 5a and b). Increased flow rate lowered the amount of wastewater treated before the bed saturated, reducing the bed's service time (Fig. 5a and b). This finding is explained by a reduction in contact time between the 2,4-D and PO$_4$$^{3-}$ ions and the AWS@Zr at higher linear flow rates. Breakthrough happens more quickly at greater flow rates, as seen in Fig. 5a and b. The column operated effectively at the lowest flow rate because the residence time of the feed solution was extended at the lower flow rate, enabling adsorbates to permeate into the pores of the adsorbent through intra-particle diffusion [21]. A high flow rate indicates that the 2,4-D and PO$_4$$^{3-}$ ions do not have enough time to diffuse into the pores of the AWS@Zr, resulting in poor uptake capacity and removal efficiency [46]. This might be due to the solute
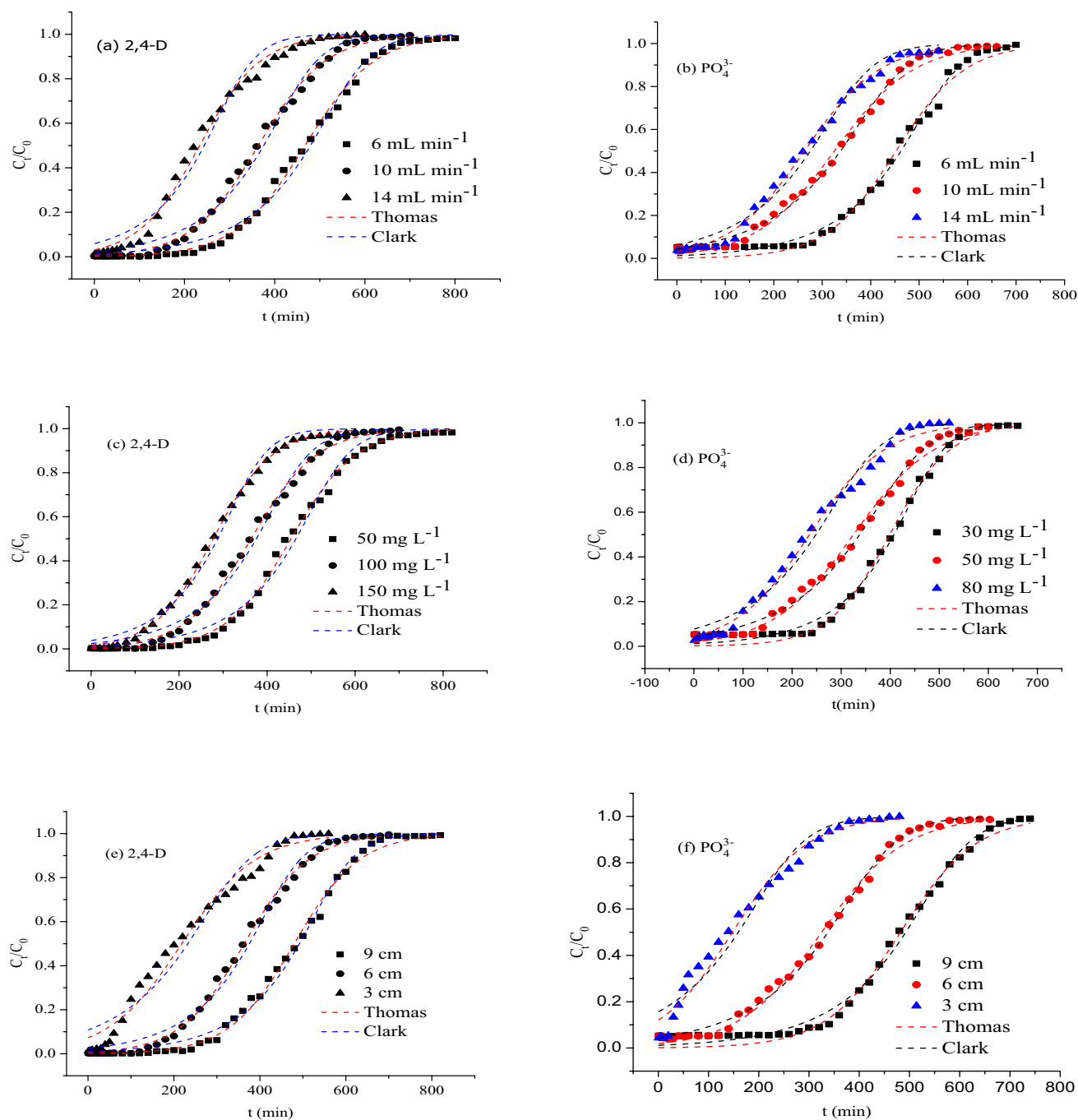
Fig. 5 Breakthrough curves of **a** 2,4-D and **b** PO_4^{3-} adsorption at various flow rates ($C_0 = 100$ mg L^{-1} for 2,4-D; $C_0 = 50$ mg L^{-1} for PO_4^{3-} at $Z = 6$ cm); **c** 2,4-D and **d** PO_4^{3-} adsorption at various con-centration ($v = 10$ mL min^{-1}; $Z = 6$ cm); **e** 2,4-D and **f** PO_4^{3-} adsorption onto AWS@Zr at various bed height ($C_0 = 100$ mg L^{-1} for 2,4-D; $C_0 = 50$ mg L^{-1} for PO_4^{3-} at $v = 10$ mL min^{-1}) onto AWS@Zr

exiting the column before equilibrium was reached [47]. It can also be observed that when the flow rate increased from 6 to 14 mL min^{-1}, the saturation time reduced from 686 to 458 min for 2,4-D; 623–497 min for PO_4^{3-}, respectively, as depicted in Table 5.

Influence of Influent Concentration on Breakthrough Curve

The impact of altering the inlet 2,4-D (50, 100, and 150 mg L^{-1}) and PO_4^{3-} (30, 50, and 80 mg L^{-1}) concentrations on the shape of the breakthrough curves was investigated at a fixed adsorbent bed depth (6 cm) and feed flow rate (10 mL min^{-1}). The resultant breakthrough curves are shown
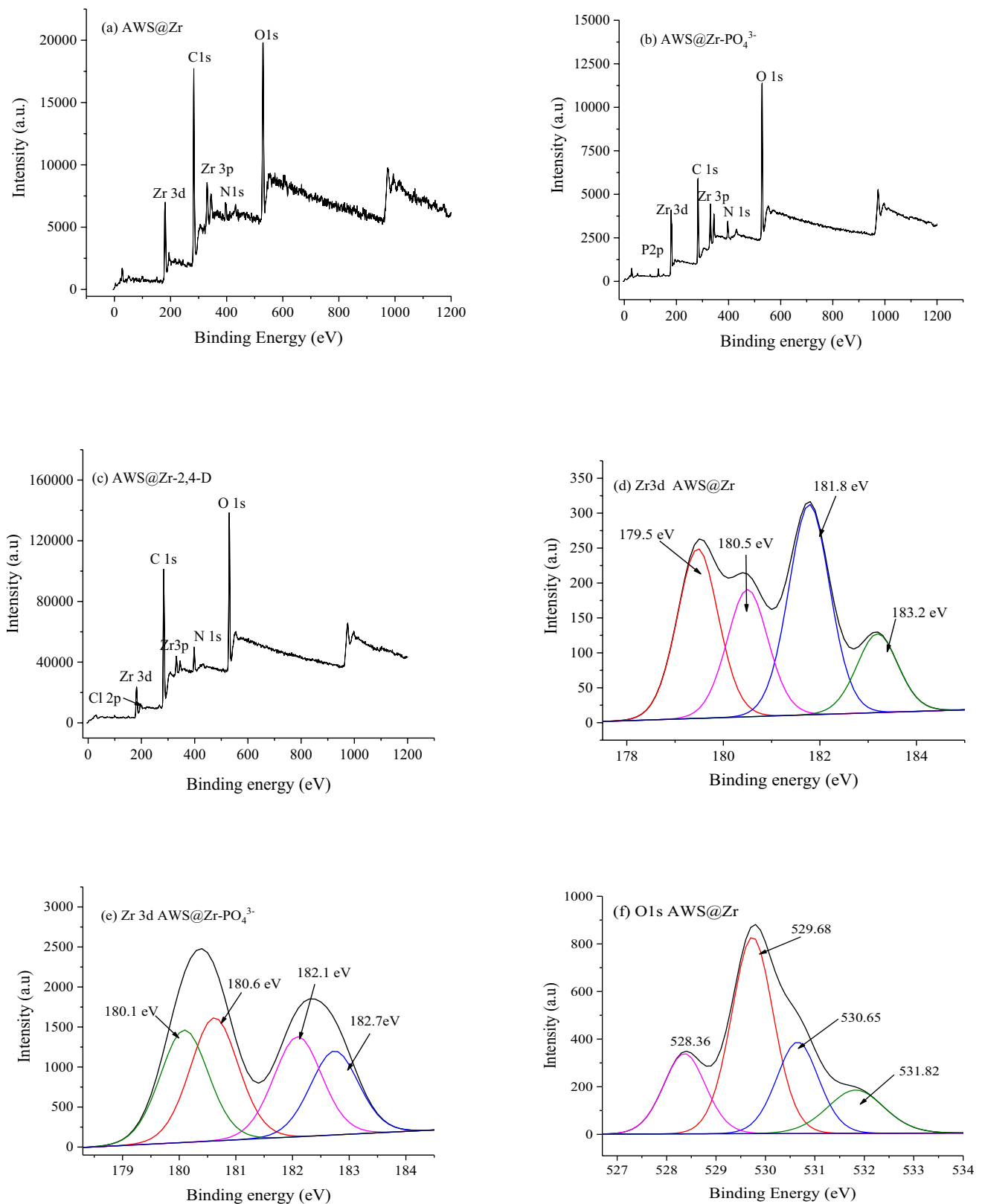
Fig. 6 XPS wide spectra **a** AWS@Zr, **b** AWS@Zr-PO_4^{3-}, **c** AWS@Zr-2,4-D. XPS high-resolution spectrum **d** Zr3*d* of AWS@Zr, **f** Zr3*d* of AWS@Zr-PO_4^{3-}, **g** O1*s* of AWS@Zr-2,4-D

(g) O 1s AWS@Zr-2,4-D
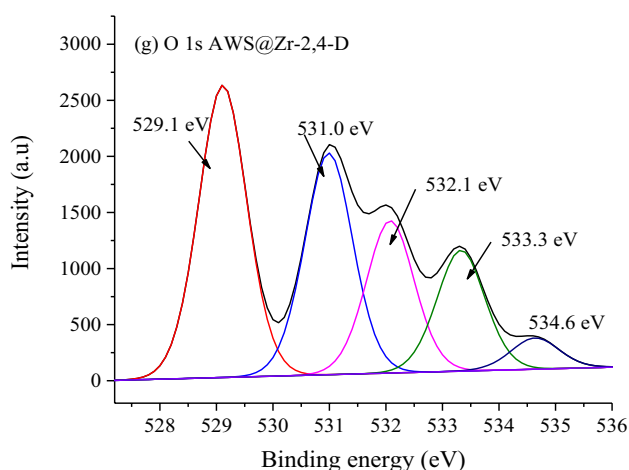
529.1 eV
531.0 eV
532.1 eV
533.3 eV
534.6 eV

Fig. 6 (continued)

in Fig. 5c and d. The graphs demonstrate that the breakthrough time reduced as the concentration of inlet adsorbates increased (Table 5). The greater the C_0 is, the steeper the breakthrough curve and the shorter the breakthrough time can be found (Fig. 5c and d). Moreover, increased inflow concentration decreased the treated volume before the bed became saturated since a high 2,4-D and PO_4^{3-} concentration may saturate the adsorbent more rapidly, reducing the operating time and vice versa. (Fig. 5c and d). The concentration gradient between the adsorbates on the adsorbent and the solution is the driving force for adsorption [21].

As a result, a high concentration offers a significant driving force for the adsorption process. However, the saturation of the adsorbent takes much longer. But, owing to the strong driving force, breakthrough occurs before all of the AWS@Zr's binding sites are covered by 2,4-D and PO_4^{3-} ions, resulting in a shortened breakthrough duration (Fig. 5c and d). The diffusion process is concentration-dependent because a change in concentration gradient affects the saturation rate and the breakthrough time [48]. In the present work, it was observed that the saturation time declined from 680 to 480 min as 2,4-D concentration increased from 50 to 150 mg L^{-1}, and a similar trend was observed for the uptake of phosphate, as illustrated in Table 5. The outcome of this research is consistent with other works reported by other researchers like Smaranda et al. [49] and Han et al. [50].

Influence of Varying Bed Heights on Breakthrough Curve

The breakthrough curves of 2,4-D and PO_4^{3-} sorption onto AWS@Zr were obtained at various bed depths with inlet concentrations of 100 mg L^{-1} and 50 mg L^{-1}, respectively, at a constant flow rate of 10 mL min^{-1} are shown in Fig. 6e and f. Three bed depths (3, 6, and 9 cm) were explored, corresponding to 0.93, 1.86, and 2.79 g dry weight of AWS@Zr, respectively. The breakthrough curves (Fig. 5e and f) reveal that as the bed depth rose from 3 to 9 cm, the breakthrough and saturation times increased. A higher bed height resulted in increased 2,4-D and PO_4^{3-} absorption (Table 3). The 2,4-D and PO_4^{3-} ions had more time to interact with the AWS@Zr particles as the bed height increased, resulting in increased 2,4-D and PO_4^{3-} adsorption in the column. Hence, as the bed height raises, the maximum adsorption capacity of the column also increases. Increasing bed depth resulted in an increase in the number of binding sites due to an increase in the adsorption surface area, which accounts

Table 5 Parameters in fixed-bed column for 2, 4-D and PO_4^{3-} uptake by AWS@Zr

C_0 (mg L^{-1})	v (mL min^{-1})	Z (cm)	q_{total} (mg)	q_{exp} (mg g^{-1})	t_b (min, $C_t/C_0 = 0.2$)	t_s (min, $C_t/C_0 = 0.96$)
2,4-D						
50	10	6	231.7	124.5	361	680
100	10	6	368.5	198.1	259	559
150	10	6	427.7	229.9	180	480
100	6	6	281.8	151.5	363	686
100	14	6	340.5	183.1	146	458
100	10	3	222.0	238.7	90	442
100	10	9	477.1	171.0	359	662
PO_4^{3-}						
30	10	6	116.6	62.7	311	559
50	10	6	160.3	86.2	198	524
80	10	6	188.5	101.3	123	422
50	6	6	131.8	70.9	364	623
50	14	6	186.2	100.1	151	497
50	10	3	78.30	84.2	41	362
50	10	9	234.6	84.1	381	669

for the enhanced 2,4-D and PO_4^{3-} absorption. With increasing bed height, the slope of the breakthrough curves became somewhat steeper, resulting in a broader mass transfer zone. When the bed depth is decreased, axial dispersion processes prevail in mass transfer, reducing the diffusion of 2,4-D and PO_4^{3-} ions. The 2,4-D and PO_4^{3-} ions did not have enough time to diffuse into the AWS@Zr bed because of the low bed depth in the column. Consequently, the overall treatment time was reduced, as well as the volume of 2,4-D and PO_4^{3-} solution treated (Fig. 5e and f). The results are similar to works reported by researchers such as Smaranda et al. [49] and Han et al. [50].

Evaluation of Applied Kinetic Column Models

The prediction of column breakthrough or the shape of the adsorption wave front, which affects the operational lifespan of the bed, is the most essential parameter in the design of fixed-bed adsorption systems. Adsorption models were extensively developed to provide a more accurate description of the behavior of pollutants in the operation of the AWS@Zr column. In this work, the modeling of the experimental data was conducted for the pollutants' adsorption by applying the Thomas and Clark models.

Thomas Model

The Thomas kinetic model was applied to the flow rate, concentration, and bed height test results. The parameters, q_0, and k_{Th} of the Thomas model were estimated employing a nonlinear regression to the experimental results, as derived from Eq. 8. Thomas model complies with Langmuir kinetics

of sorption–desorption. As shown in Table 6, the values of the Thomas constant k_{Th} reduce as the concentrations of all pollutants tested (2,4-D, and PO_4^{3-}) increased. It was also revealed that when the pollutant concentration in the influent increased, the absorption capacity of AWS@Zr in the column, q_0, calculated using the Thomas model, improved. This finding is based on the fact that the difference in concentration between the solid and liquid phases acts as a driving force for pollutant molecule retention. The column efficiency was increased as a result of the higher driving force induced by the increased pollutant concentration [21, 50].

As a result, it is shown that at high concentrations and low influent feed flow rate, adsorbate adsorption onto the AWS@Zr in the column is maximized. The R^2 values from Thomas and Clark were highly substantial, indicating that they could equally explain the adsorption of all contaminants onto AWS@Zr as shown in Tables 6 and 7. However, the Thomas model best predicted the uptake phenomena of 2, 4-D and PO_4^{3-} based on high R^2 and lower SSE values obtained (Tables 6 and 7). These findings generally agree with those found during the uptake of dye onto soil [49].

Clark Model

The Clark model's parameters A and r were derived via nonlinear regression analysis using Eq. (9), and the results are shown in Table 7. The values of the mass transfer rate "r" increase with increasing flow velocity, as shown in Table 7; this is due to the shorter distance for molecular diffusion of the adsorbate through the stationary zone of liquid surrounding the adsorbent [51]. On the other hand, when the flow rate rose and the adsorbate concentration increased,

Table 6 Parameters of Thomas model for 2,4-D, and PO_4^{3-} adsorption at different conditions

Thomas							
C_0 (mg L^{-1})	v (mL min^{-1})	Z (cm)	k_{Th} (mL mg^{-1} min^{-1})	q_{exp} (mg g^{-1})	q_0 (mg g^{-1})	R^2	SSE
2,4-D							
50	10	6	0.273 ± 0.005	124.5	122.2 ± 0.4	0.998	0.012
100	10	6	0.134 ± 0.003	198.1	195.5 ± 1.0	0.998	0.013
150	10	6	0.0994 ± 0.0016	229.9	223.8 ± 1.0	0.999	0.0066
100	6	6	0.129 ± 0.003	151.5	150.7 ± 0.6	0.998	0.014
100	14	6	0.148 ± 0.005	183.1	175.9 ± 2.1	0.994	0.032
100	10	3	0.117 ± 0.006	238.7	234.5 ± 5.3	0.982	0.075
100	10	9	0.132 ± 0.003	171.0	172.0 ± 0.7	0.997	0.020
PO_4^{3-}							
30	10	6	0.539 ± 0.021	62.7	64.4 ± 0.4	0.993	0.035
50	10	6	0.243 ± 0.007	86.2	87.4 ± 0.7	0.995	0.024
80	10	6	0.163 ± 0.005	101.3	101.3 ± 1.2	0.993	0.026
50	6	6	0.280 ± 0.012	70.9	72.9 ± 0.5	0.990	0.050
50	14	6	0.257 ± 0.006	100.1	99.1 ± 0.7	0.997	0.012
50	10	3	0.270 ± 0.014	84.2	79.4 ± 2.3	0.981	0.060
50	10	9	0.268 ± 0.010	84.1	86.4 ± 0.6	0.992	0.042

Table 7 Parameters of Clark model for 2,4-D and PO_4^{3-} adsorption at different conditions

Clark							
C_0 (mg L^{-1})	v (mL min^{-1})	Z (cm)	$A \times 10^3$	$r \times 10^{-3}$	n	R^2	SSE
2,4-D							
50	10	6	184.3 ± 82.3	22.4 ± 0.9	3.69	0.993	0.0529
100	10	6	216.8 ± 7.7	22.1 ± 0.9	3.69	0.992	0.0480
150	10	6	6.96 ± 2.30	24.9 ± 1.1	3.69	0.992	0.0429
100	6	6	149.0 ± 56.9	21.3 ± 0.8	3.69	0.994	0.0415
100	14	6	2.052 ± 0.851	24.3 ± 1.6	3.69	0.981	0.0995
100	10	3	0.400 ± 0.141	18.5 ± 1.4	3.69	0.965	0.144
100	10	9	248.6 ± 80.6	21.8 ± 0.6	3.69	0.996	0.0270
PO_4^{3-}							
30	10	6	245.7 ± 94.3	26.1 ± 0.9	3.77	0.995	0.0242
50	10	6	5.72 ± 0.44	20.4 ± 0.4	3.77	0.997	0.0140
80	10	6	1.215 ± 0.359	21.5 ± 1.1	3.77	0.985	0.0597
50	6	6	207.3 ± 77.8	22.7 ± 0.8	3.77	0.994	0.0322
50	14	6	2.200 ± 0.626	21.6 ± 1.0	3.77	0.988	0.0475
50	10	3	0.171 ± 0.049	21.2 ± 1.6	3.77	0.967	0.107
50	10	9	237.5 ± 90.1	21.6 ± 0.7	3.77	0.993	0.0354

the 'A' values declined. The findings corroborated the studies conducted [51]. Again, as seen in Tables 6 and 7, R^2 and the corresponding SSE values were significant which suggest to predict the adsorption process of 2,4-D and PO_4^{3-} onto AWS@Zr. The findings indicated that the uptake of adsorbates onto the adsorbent followed both monolayer and multilayer adsorption process since Thomas and Clark models complies with Langmuir and Freundlich models, respectively.

Column Isotherm Modeling

The equilibrium reaction between distributed molecules in a solution and the adsorbent is described by an adsorption isotherm. Batch experiment results were insufficient to illustrate column phase equilibrium. Hence, C_{eff} is described in Eq. (19).

$$C_{eff} = \frac{m_{Total} - q_{Total}}{V_{eff}} \tag{19}$$

Then, q_e at a specific effluent time was estimated as well. As a result, the plot of q_e against C_{eff}, comparable to the batch studies, is shown in Fig. S4a (2,4-D) and Fig. S4b (PO_4^{3-}). To estimate the isotherm parameters of the experimental column findings, the Langmuir and Freundlich isotherm models were used [29]. Table 8 and Fig. S4a and S4b present the parameters obtained from the isotherm models and the fitted curves for the column results, respectively. It can be observed that the Langmuir isotherm model best represented the adsorption phenomena

since it exhibited higher R^2 and lower SSE values for the adsorption of all the adsorbates (2,4-D, and PO_4^{3-}) compared to the Freundlich model. Additionally, it is necessary to understand that the Langmuir adsorption isotherm best fits both batch and experimental column data.

Mass Transfer Factor

A graph of $\ln q$ vs $\ln t$ depicts a straight line having B as an intercept with β^{-1} as a slope. The correlation coefficient relating to all adsorbate adsorption was sufficiently high, as shown in Table S1, suggesting that employing the index B and β^{-1} obtained from Eq. (6) is favorable for estimating the mass transfer potential and affinity between adsorbate and AWS@Zr. As depicted in Table S1, for the adsorption of 2,4-D and PO_4^{3-}, the index B increased as their concentrations increased due to a greater driving force for 2,4-D and PO_4^{3-} adsorption into AWS@Zr. Moreover, the values of β^{-1} reduced as the concentration of all the adsorbate increased, as presented in Table S1, which indicates that the variation between the values of β^{-1} is significant enough to distinguish between the forces of attraction that define pollutants' removal preferences [20]. Experimental data validation shows the increase of attractive forces for adsorption of $PO_4^{3-} > 2,4$-D onto AWS@Zr based on β^{-1} value presented in Table S1.

Column Regeneration and Reuse

Regenerating a depleted AWS@Zr is a significant achievement because it optimizes the cost-effectiveness of the

Table 8 Column isotherms parameters for adsorption studied pollutants onto AWS@Zr

C_0 (mg L^{-1})	50	100	150
2,4-D			
Freundlich isotherm			
K_F (mg g^{-1}) (L mg^{-1})$^{1/n}$	63.5 ± 4.4	73.9 ± 6.3	63.7 ± 5.4
$1/n$	0.254 ± 0.028	0.278 ± 0.026	0.309 ± 0.022
R^2	0.891	0.933	0.967
SSE $\times 10^2$	37.1	50.2	27.3
Langmuir isotherm			
K_L (L mg^{-1})	2.15 ± 0.33	0.651 ± 0.069	0.196 ± 0.023
q_m (mg g^{-1})	123.5 ± 3.5	197.0 ± 4.7	237.2 ± 5.5
R^2	0.959	0.975	0.984
SSE $\times 10^2$	14.0	18.3	13.4
C_0 (mg L^{-1})	30	50	80
PO$_4^{3-}$			
Freundlich isotherm			
K_F (mg g^{-1}) (L mg^{-1})$^{1/n}$	16.7 ± 2.8	14.9 ± 2.6	13.5 ± 2.3
$1/n$	0.606 ± 0.090	0.606 ± 0.071	0.562 ± 0.050
R^2	0.686	0.816	0.883
SSE $\times 10^2$	34.9	34.0	27.2
Langmuir isotherm			
K_L (L mg^{-1})	0.173 ± 0.061	0.0887 ± 0.0232	0.0544 ± 0.0101
q_m (mg g^{-1})	105.3 ± 20.4	140.0 ± 19.0	152.2 ± 13.3
R^2	0.745	0.869	0.930
SSE $\times 10^2$	28.30	24.21	16.31

adsorbent. Based on the desorption efficiency attained in the batch experiment, the 2,4-D loaded adsorbents were desorbed using 0.1 mol L^{-1} NaOH, while the PO$_4^{3-}$ loaded adsorbent was regenerated with a 0.1 mol L^{-1} mixture of NaOH/NaCl. The results are shown in Fig. S4c and S4f. The elution curves seen in all cases follow a similar trend. The concentration of pollutants in the effluents was quite high at the beginning of the desorption process but quickly fell to a very low concentration as the process continued. The maximum concentrations of adsorbates desorbed for the first and second cycles were 3043 mg L^{-1} and 3082 mg L^{-1} for 2,4-D; 88.6 mg L^{-1} and 99 mg L^{-1} for PO$_4^{3-}$, respectively. The high desorption performance could be linked to the capacity of the desorbing solvent ions to disrupt the force of interaction between AWS@Zr and studied pollutants through ion-exchange phenomena.

Furthermore, there was no substantial change in desorption efficiency for desorption cycles. Table 9 shows the t_b, q_0, and %R for two successive adsorption–desorption cycles. The %R values declined slightly as the procedure continued, as seen in Table 9.

This performance might be assigned to the binding site on the adsorbent being regenerated in the desorption solution. Again, it could be linked to the fact that some of the active sites were underutilized during the adsorption process, which took part in the uptake during the regeneration section. The findings show that the AWS@Zr may be utilized for further pollutant adsorption even after two cycles. As a result, AWS@Zr is a promising adsorbent with substantial potential for removing pollutants from effluents.

Table 9 Adsorption–desorption parameters for studied pollutants using AWS@Zr

| Adsorbate	2,4-D			PO$_4^{3-}$		
Cycle	q_0 (mg g^{-1})	t_b (min) at $C_t/C_0 = 0.2$	R %	q_0 (mg g^{-1})	t_b (min) at $C_t/C_0 = 0.2$	R %
Initial	198.1	259		86.2	198	
First	186.3	231	94.0	69.9	147	81.1
Second	166.1	184	89.2	64.6	137	74.9

Adsorption Mechanisms

The XPS studies were carried out to understand the underlying reaction process during the removal of 2,4-D and PO_4^{3-} onto AWS@Zr. The wide scan of AWS@Zr before and after the uptake of PO_4^{3-} and 2,4-D is presented in Fig. 6a–c, respectively. The emergence of Zr$3d$ peaks confirmed the successful loading of Zr (VI) onto the adsorbent. Again, the Zr$3d$ peaks exhibited two main splits at ~179.50 and ~183.20 eV, representing Zr$3d_{5/2}$ and Zr $3d_{3/2}$, respectively. The deconvolution of Zr3d of AWS@Zr gave four peaks at 179.50, 180.50, 181.80, 183.20 eV relating to Zr–C, Zr–O, Zr–Zr, Zr–O, respectively, as presented in Fig. 6d. Moreover, upon the uptake of phosphate as depicted in Fig. 7e, the deconvolution of Zr3d of AWS@Zr–PO_4^{3-} gave peaks at 179.9, 180.6, 182.1 and 182.7 eV corresponding to Zr–C and Zr–O bonds. The shift exhibited in some of the peaks may be due the uptake of phosphate onto AWS@Zr. The high-resolution spectrum of O1s of AWS@Zr before Fig. 6f and after adsorption of 2,4-D Fig. 6g was estimated. As shown in Fig. 6e, the O1s on AWS@Zr prior to uptake yielded peaks at 528.36, 529.68, 530.65, and 531.82 eV matching to Zr-O, O=C–OH, OH/O–Zr, and H_2O bonds, respectively [15, 18, 52]. Then, after the uptake of 2,4-D, the O1s of AWS@Zr gave peaks at 529.1, 531.0, 532.1, 533.3 and 534.6 eV representing Zr–O, Zr–OH, C–O=O, and H_2O as depicted in Fig. 6g. The slight shift in the peaks of O1s of AWS@Zr could be attributed to uptake of the 2,4-D molecules. The existence of Zr–O peaks in the spectra of Zr3d of AWS@Zr after the uptake of PO_4^{3-} (Fig. 6e) and the O1s of AWS@Zr after 2,4-D adsorption (Fig. 6g) could be partially ascribed to the bonds formed between Zr and the pollutants (PO_4^{3-} and 2,4-D) [33]. Again, the appearance of Cl2p peaks for spent AWS@Zr increasing from 1.88 to 3.58% further indicated that 2,4-D was successfully adsorbed (Fig. 6c). Furthermore, analysis reveals that Zr present on AWS@Zr decreased from 2.82 to 1.75% and 1.08% after the adsorption of 2,4-D and PO_4^{3-}, respectively, this may be ascribed to the active involvement of Zr in the removal process. The proposed removal mechanism is illustrated in Fig. 7.

Conclusion

The synthesized adsorbent, AWS@Zr was prepared through incorporation of Zirconium onto the amino-grafted walnut shell. The AWS@Zr adsorbent was effectively used to remediate 2,4-D and phosphate via batch and column mode. The Langmuir model characterized the adsorption phenomena of 2,4-D, while both Temkin and Freundlich model could describe the uptake of phosphate. This implies that the adsorption model assumes that adsorption is a multi-layer process characterized by uniform aggregation of binding energies, up to maximum binding energy. The pseudo-second-order fits the kinetics studies, while the Thomas model predicted the breakthrough curves. Experimental data reveal the increase of attractive forces for adsorption of PO_4^{3-} was higher than 2,4-D onto AWS@Zr based on β^{-1} value and competitive adsorption. Electrostatic interaction and complex formation could be the key mechanisms underpinning studied pollutants adsorption. The AWS@Zr adsorbent displayed high reusability, suggesting its practical applicability in removing chemical pollutants from wastewater. The

Fig. 7 Proposed reaction mechanisms
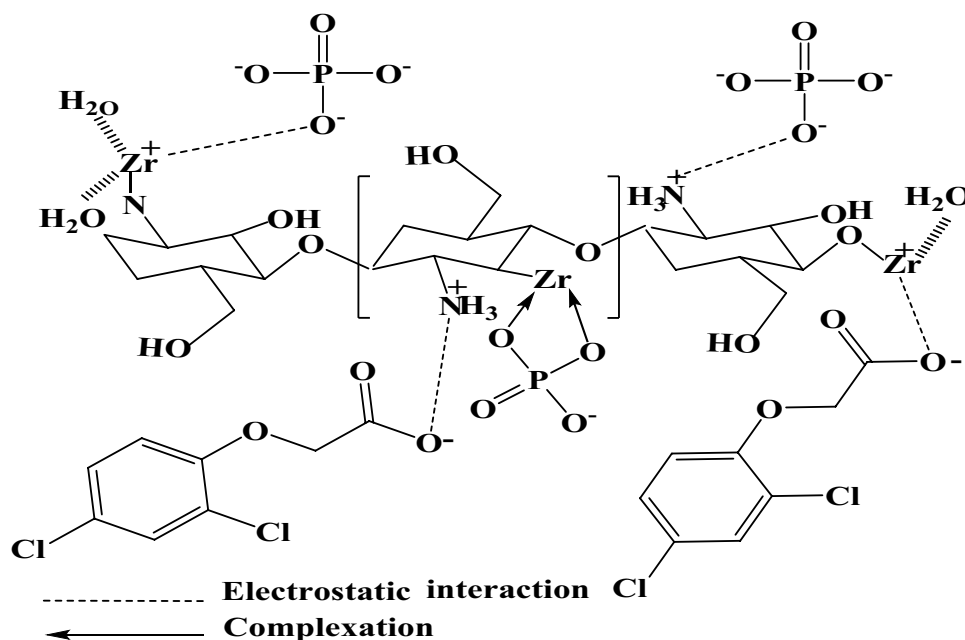
presence of salt ions impacted negatively on the adsorption phenomena.

References

1. S.A.R. Khan, P. Ponce, Z. Yu, H. Golpira, M. Mathew, Chemosphere **286**, 131532 (2021)
2. M. Ponnuchamy, A. Kapoor, P. Senthil, K. Dai, V.N. Vo, Environ. Chem. Lett. **19**, 2425 (2021)
3. K. Kuśmierek, M. Szala, A. Świątkowski, J. Taiwan Inst. Chem. E. **63**, 371 (2016)
4. N.A. Baharum, H.M. Nasir, M.Y. Ishak, M. Isa, M.A. Hassan, A.Z. Aris, Arab. J. Chem. **13**, 6106 (2020)
5. S. Cosgrove, B. Jefferson, P. Jarvis, Environ. Technol. Rev. **8**, 1 (2019)
6. R. Awual, J. Clean. Prod. **228**, 1311 (2019)
7. V.H. Smith, Environ. Sci. Pollut. Res. **10**, 126 (2003)
8. D.M. Anderson, P.M. Glibert, J.M. Burkholder, Estuaries **25**, 704 (2022)
9. F.M. Mpatani, A.A. Aryee, R.P. Han, Z.H. Li, E. Dovi, L.B. Qu, J. Clean. Prod. **308**, 127359 (2021)
10. A.N. Kani, E. Dovi, F.M. Mpatani, A.A. Aryee, R.P. Han, Z.H. Li, L.B. Qu, Environ. Chem. Lett. **20**, 705 (2022)
11. F.M. Mpatani, R.P. Han, A.A. Aryee, A.N. Kani, L.B. Qu, Z.H. Li, Sci. Total. Environ. **780**, 146629 (2021)
12. G.L. Dotto, G. McKay, J. Environ. Chem. Eng. **8**, 103988 (2020)
13. X. Xu, B.Y. Gao, B. Jin, Q.Y. Yue, J. Mol. Liq. **215**, 565 (2016)
14. A.A. Aryee, F.M. Mpatani, A.N. Kani, E. Dovi, R.P. Han, Z.H. Li, L.B. Qu, J. Clean. Prod. **310**, 127502 (2021)
15. A.A. Aryee, E. Dovi, X.X. Shi, R.P. Han, Z.H. Li, L.B. Qu, Colloid. Surface. A **615**, 126260 (2021)
16. M.Y. Liu, Z.Y. Zang, S.S. Zhang, G.F. Ouyang, R.P. Han, Int. J. Biol. Macromol. **182**, 1759 (2021)
17. J.L. Wang, X. Liu, H.Y. Han, R.P. Han, Korean J. Chem. Eng. **40**, 1970 (2023)
18. Y.Y. Hu, R.P. Han, J. Chem. Eng. Data **64**, 791 (2019)
19. E. Dovi, A.A. Aryee, M.Y. Liu, X.T. Zhang, A.N. Kani, J.J. Li, R.P. Han, L.B. Qu, Environ. Sci. Pollut. Res. **29**, 90530 (2022)
20. M.A. Fulazzaky, M. Nuid, A. Aris, M. Fulazzaky, K. Sumeru, J. Water Process. Eng. **31**, 100889 (2019)
21. Z. Akzu, F. Gonen, Process Biochem. **39**, 599 (2004)
22. R.M. Clark, Environ. Sci. Technol. **21**, 573 (1987)
23. Z. Ren, X. Xu, X. Wang, B.Y. Gao, Q.Y. Yue, W. Song, H. Wang, J. Colloid Interface Sci. **468**, 313 (2016)
24. J. Ayala, B. Fernández, Environ. Prot. Eng. **45**, 141 (2019)
25. Y. Waktole, B. Seid, T. Mereta, F. Fufa, Appl Water Sci **9**(2), 1 (2019)
26. T. Zhou, L.Y. Fang, X.W. Wang, M.Y. Han, S.S. Zhang, R.P. Han, Desalin. Water Treat. **70**, 294 (2017)
27. J.S. Cao, J.X. Lin, F. Fang, M.T. Zhang, Z.R. Hu, Bioresour. Technol. **163**, 199 (2014)
28. N. Ayawei, A.N. Ebelegi, D. Wankasi, J. Chem. **2017**, 3039817 (2017)
29. R.P. Han, L.J. Zhang, C. Song, M.M. Zhang, H.M. Zhu, L.J. Zhang, Carbohyd. Polym. **79**, 1140 (2010)
30. Y.S. Ho, G. Mckay, Process Biochem. **34**, 451 (1999)
31. W. Zhang, H. Li, X. Kan, L. Dong, H. Yan, Z. Jiang, R. Cheng, Bioresour. Technol. **117**, 40 (2012)
32. F. Fu, Z. Gao, L. Gao, D. Li, Ind. Eng. Chem. Res. **50**, 9712 (2011)
33. Y.F. Gu, M.M. Yang, W.L. Wang, R.P. Han, J. Chem. Eng. Data **64**, 2849 (2019)
34. U. Herrera-García, J. Castillo, D. Patiño-Ruiz, R. Solano, A. Herrera, Water **11**(11), 2342 (2019)
35. J. Goscianska, A. Olejnik, Adsorption **25**(3), 345 (2019)
36. H.K. Hue, L.V. Anh, D.B. Trong, Vietnam J. Chem. **56**, 208 (2018)
37. S. Şahin, S. Emik, J. Mol. Liq. **260**, 195 (2018)
38. W. Liu, Q. Yang, Z. Yang, W. Wang, Colloid Surf. A **509**, 367 (2016)
39. T.L. Eberhardt, S. Min, J.S. Han, Bioresour. Technol. **97**, 2371 (2006)
40. A.A. Aryee, F.M. Mpatani, X. Zhang, A.N. Kani, E. Dovi, R.P. Han, Z.H. Li, L.B. Qu, J. Clean. Prod. **268**, 122191 (2020)
41. G. Peng, S. Jiang, Y. Wang, Q. Zhang, Y. Cao, Y. Sun, L. Wang, J. Clean. Prod. **251**, 119725 (2020)
42. A.A. Aryee, R.P. Han, L.B. Qu, J. Environ. Chem. Eng. **11**, 111281 (2023)
43. L.Z. Han, P.G. Qin, M.Y. Li, D. Li, M.Y. Mu, Y.M. Gao, S.P. Zhu, M.H. Lu, Z.W. Cai, Chem. Eng. J. **456**, 140969 (2023)
44. X.T. Zhang, S.S. Zhang, G.F. Ouyang, R.P. Han, Korean J. Chem. Eng. **39**, 1839 (2022)
45. J. Mittal, A. Mariyam, F. Sakina, R.T. Baker, A.K. Sharma, A. Mittal, J. Clean. Prod. **321**, 129060 (2021)
46. D.C.K. Ko, J.F. Porter, G. Mckay, Chem. Eng. Sci. **55**, 5819 (2000)
47. T.S. Singh, K.K. Pant, Sep. Purif. Technol. **48**(3), 288 (2006)
48. M.K. Mondal, J. Environ. Manag. **90**, 3266 (2009)
49. C. Smaranda, M. Popescu, D. Bulgariu, T. Măluţan, M. Gavrilescu, Process. Saf. Environ. Prot. **108**, 108 (2016)
50. R.P. Han, Y. Wang, X. Zhao, Y.F. Wang, F.L. Xie, J.M. Cheng, M.S. Tang, Desalination **245**, 284 (2009)
51. X.F. Sun, T. Imai, M. Sekine, T. Higuchi, K. Yamamoto, A. Kanno, S. Nakazono, J. Ind. Eng. Chem. **20**, 3623 (2014)
52. M.Y. Liu, X.T. Zhang, Z.H. Li, L.B. Qu, R.P. Han, Carbohydr. Polym. **248**, 116792 (2020)